Tellus
SERIES A
DYNAMIC
METEOROLOGY
AND OCEANOGRAPHY
PUBLISHED BY THE INTERNATIONAL METEOROLOGICAL INSTITUTE IN STOCKHOLM

Tellus (2009), 61A, 621–630
Printed in Singapore. All rights reserved

TELLUS

An unconventional approach for assimilating aliased radar radial velocities

By QIN XU[1]*, KANG NAI[2], LI WEI[2] and QINGYUN ZHAO[3], [1]*NOAA/National Severe Storms Laboratory, Norman, OK, USA;* [2]*Cooperative Institute for Mesoscale Meteorological Studies, University of Oklahoma, Norman, OK, USA;* [3]*Naval Research Laboratory, Monterey, CA, USA*

(Manuscript received 22 April 2009; in final form 22 July 2009)

ABSTRACT

An aliasing operator is introduced to mimic the effect of aliasing that causes discontinuities in radial-velocity observations, and to modify the observation term in the costfunction for direct assimilations of aliased radar radial-velocity observations into numerical models. It is found that if the aliasing operator is treated as a part of the observation operator and applied to the analysed radial velocity in a conventional way, then the analysis is not ensured to be aliased (or not aliased) in consistency with the aliased (or not aliased) observation at every observation point. Thus, the analysis-minus-observation term contains a large alias error whenever an inconsistency occurs at an observation point. This causes fine-structure discontinuities in the costfunction. An unconventional approach is thus introduced to apply the aliasing operator to the entire analysis-minus-observation term at each observation point in the observation term of the costfunction. With this approach, the costfunction becomes smooth and concave upwards in the vicinity of the global minimum. The usefulness of this approach for directly assimilating aliased radar radial-velocity observations under certain conditions is demonstrated by illustrative examples.

1. Introduction

It is well known in radar meteorology (Doviak and Zrnić, 2006) that each radial-velocity measurement is determined from the observed echo phase difference between successive transmitted pulses, so there is a maximum velocity, called the Nyquist velocity, v_N, beyond which the measured radial velocities are aliased back into the Nyquist interval between $\pm v_N$. The observed radial velocity v_r^o is thus related to the true v_r by

$$v_r^o = Z\left[v_r + \varepsilon^o, v_N\right], \tag{1}$$

where $Z[(\ ), v_N] = (\ ) - 2v_N N[(\ ), v_N]$ is the aliasing operator, $N[(\ ), v_N] = \mathrm{Int}[(\ )/(2v_N)]$ is the Nyquist number of ( ), $\mathrm{Int}[(\ )/(2v_N)]$ represents the nearest integer of $(\ )/(2v_N)$, and ε^o denotes the random measurement error (other than the aliasing error). Clearly, $Z[(\ ), v_N]$ is a piecewise-linear and zigzag-discontinuous function of ( ) (see e.g. Doviak and Zrnić, 2006; their fig. 7.9), and the Nyquist number N is an integer indeterminable from the aliased velocity.

Radar radial-velocity aliasing usually can be detected from abrupt velocity changes of about $2v_N$ between neighbouring measurements, but correcting aliased velocities is nontrivial and often requires additional independent wind information to provide some reference points (Ray and Ziegler, 1977; Hennington, 1981; Bergen and Albers, 1988). Because aliasing can occur in countless different ways and the aliasing scenarios can be extremely complex, dealiasing has been an indispensable and yet often very difficult step in the radar data quality control. Considerable efforts have been made in developing various techniques to correct aliased velocities (Eilts and Smith, 1990; Jing and Wiener, 1993; Yamada and Chong, 1999; James and Houze, 2001; Tabary et al., 2001; Gong et al., 2003; Haase and Landelius, 2004; Gao et al., 2004; Zhang and Wang, 2006). The techniques so far developed, however, are still not sufficiently robust to deal with every severely aliased situation and correct or flag all aliased radar radial velocities. To meet the high-quality standard required by radar data assimilation for numerical weather predictions, increasingly comprehensive algorithms need to be developed to deal with various aliasing scenarios. In addition to the common approach that treats dealiasing as a part of radar data quality control, it is also possible and perhaps more effective to modify the costfunction to directly assimilate aliased radial-velocity observations. This approach is explored in this paper. In particular, by incorporating the aliasing operator into the costfunction, aliased radar radial-velocity observations can be assimilated directly to reduce the dealiasing burden on radar data quality control or even to skip the dealiasing step in radar data quality control. This approach is introduced in Section 2

---

*Corresponding author.
e-mail: qin.xu@noaa.gov
DOI: 10.1111/j.1600-0870.2009.00412.x

by comparing two different ways of incorporating the aliasing operator into the costfunction. The usefulness and limitation of the proposed approach for assimilating aliased radial velocities are demonstrated by illustrative examples with both simulated and real radar observations in Section 3. Conclusions follow in Section 4.

2. Two ways of incorporating the aliasing operator into the costfunction

2.1. Modifying the observation operator

The true radial velocity v_r in (1) is the projection of the mean (spatially weighted within each resolution volume of the radar scan; Doviak and Zrnić, 2006; their section 5.2) vector velocity of meteorological scatterers (mainly hydrometeors), denoted by $\mathbf{v}_h = \mathbf{v}_a - w_T\mathbf{k}$, onto the radar beam direction, where $\mathbf{v}_a = (u, v, w)$ is the air velocity, w_T is the hydrometeors' terminal velocity (Doviak and Zrnić, 2006; their section 8.2) and $\mathbf{k}$ is the vertical unit vector. This projection gives

$$v_r = \mathbf{h}^T\mathbf{v}_h, \tag{2}$$

where $\mathbf{h}^T = (\sin\phi\cos\theta, \cos\phi\cos\theta, \sin\theta)$ is the observation operator that projects $\mathbf{v}_h$ onto the radial direction at a given observation point, $(\;)^T$ denotes the transpose of $(\;)$, θ is the elevation angle, ϕ is the azimuthal angle (clockwise with respect to the y-coordinate pointing to the north). The background (provided by the model prediction) and analysis increment of $\mathbf{v}_h$ can be denoted by $\mathbf{v}_h^b$ and $\Delta\mathbf{v}_h$, respectively, so their projections onto the radar beam direction are $v_r^b = \mathbf{h}^T\mathbf{v}_h^b$ and $\Delta v_r = \mathbf{h}^T\Delta\mathbf{v}_h$, respectively, in consistency with (2).

When the observed radial velocities are free of aliases, the random observation error ε^o in (1) is mainly due to the radar receiver noise and sampling error. Although observation errors are correlated between adjacent resolution volumes (represented by observation points) on each tilt of the radar scan, the error de-correlation length scale is very short (Xu et al., 2007). For simplicity, we can assume that the radar observation errors are uncorrelated between different observation points. In this case, the observation term in the costfunction for radar radial velocity assimilation has the following form:

$$J_o = \sigma_o^{-2}\sum_i \left(v_r^a - v_r^o\right)_i^2, \tag{3}$$

where σ_o^2 is the observations error variance, $v_r^a = v_r^b + \Delta v_r = \mathbf{h}^T(\mathbf{v}_h^b + \Delta\mathbf{v}_h)$ is the analysed radial velocity, and $(\;)_i$ denotes the value of $(\;)$ at the ith observation point.

When the observed radial velocities are not free of aliases, each observed v_r^o is related to the true radial velocity through the aliasing operator as shown in (1), so the observation term J_o in (3) must be modified accordingly. One way to do this is to treat the aliasing operator as a part of the observation operator without altering the conventional form of the observation term in the costfunction [e.g. eq. (2.1) of Parrish and Derber, 1992; Daley and Barker, 2001], so the observation operator $\mathbf{h}^T$ in (2) is modified into $Z[\mathbf{h}^T(\;), v_N]$ and the observation term J_o in (3) becomes

$$J_{o1} = \sigma_o^{-2}\sum_i \left(Z\left[v_r^a, v_N\right] - v_r^o\right)_i^2. \tag{4}$$

Note that $Z[v_r^a, v_N] = v_r + \Delta v_r + \varepsilon^b - 2v_N N[v_r^a, v_N]$, where $v_r^a = v_r^b + \Delta v_r = v_r + \Delta v_r + \varepsilon^b$ is used and ε^b denotes the background error. Substituting this and (1) into the analysis-minus-observation term in (4) gives

$$\begin{aligned} Z\left[v_r^a, v_N\right] - v_r^o = \Delta v_r + \varepsilon^b - \varepsilon^o - 2v_N\big(N\left[v_r^a, v_N\right] \\ -N\left[v_r + \varepsilon^o, v_N\right]\big). \end{aligned} \tag{5}$$

This result shows that $Z[v_r^a, v_N]$ cannot fit v_r^o correctly unless $N[v_r^a, v_N] = N[v_r + \varepsilon^o, v_N]$. The latter condition, however, is not always satisfied, so the modified observation term J_{o1} in (4) cannot ensure the correctness of the fitting at each observation point. For example, if v_r^a and $v_r + \varepsilon^o$ are both very close to v_N but $v_r^a < v_N < v_r + \varepsilon^o$ at an observation point, then $N[v_r^a, v_N] \neq N[v_r + \varepsilon^o, v_N]$ and a small increase of Δv_r can cause the analysis-minus-observation term in (5) to jump at that observation point. This implies that J_{o1} in (4) is not a continuous function of $(v_r^a)_i$ or $(\Delta v_r)_i$, as will be illustrated in Section 3.

2.2. Modifying the analysis-minus-observation term

As a second way or unconventional approach, the aliasing operator can be also applied to the entire analysis-minus-observation term, that is, $v_r^a - v_r^o$ at each observation point (rather than merely to v_r^a). In this case, the observation term J_o in (3) is modified into

$$J_{o2} = \sigma_o^{-2}\sum_i \left(Z\left[v_r^a - v_r^o, v_N\right]\right)_i^2. \tag{6}$$

Note that $v_r^a - v_r^o = \Delta v_r + \varepsilon^b - \varepsilon^o + 2v_N N[v_r + \varepsilon^o, v_N]$. Substituting this and the aliasing operator into the analysis-minus-observation term in (6) gives

$$\begin{aligned} Z\left[v_r^a - v_r^o, v_N\right] &= v_r^a - v_r^o - 2v_N N\left[v_r^a - v_r^o, v_N\right] \\ &= \Delta v_r + \varepsilon^b - \varepsilon^o + 2v_N N[v_r + \varepsilon^o, v_N] \\ &\quad - 2v_N N\left(\Delta v_r + \varepsilon^b - \varepsilon^o + 2v_N N\left[v_r + \varepsilon^o, v_N\right], v_N\right) \\ &= \Delta v_r + \varepsilon^b - \varepsilon^o - 2v_N N\left[\Delta v_r + \varepsilon^b - \varepsilon^o, v_N\right], \end{aligned} \tag{7}$$

where $N(\Delta v_r + \varepsilon^b - \varepsilon^o + 2v_N N[v_r + \varepsilon^o, v_N], v_N) = N[\Delta v_r + \varepsilon^b - \varepsilon^o, v_N] + N[v_r + \varepsilon^o, v_N]$ is used. From (7), it is apparent that

$$Z\left[v_r^a - v_r^o, v_N\right] = \Delta v_r + \varepsilon^b - \varepsilon^o \text{ as long as } \left|\Delta v_r + \varepsilon^b - \varepsilon^o\right| < v_N. \tag{8}$$

Thus, the observation term J_{o2} in (6) is a continuous function of $(v_r^a)_i$ or $(\Delta v_r)_i$ if $|\Delta v_r + \varepsilon^b - \varepsilon^o| < v_N$ at the ith observation point. As will be illustrated in Section 3, this property ensures

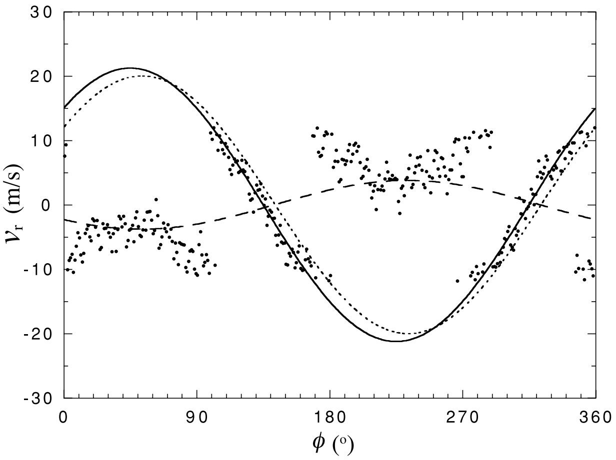

Fig. 1. Simulated true radial velocity plotted as a function of azimuth ϕ by the solid curve. The dots are the simulated radial-velocity observations. The dotted and dashed curves are the radial velocities computed by $v_r^a = \mathbf{h}^T\mathbf{v}^a$ for $\mathbf{v}^a = (16, 12)^T$ and $(-3.0, -2.3)^T$ m s^{-1}, respectively. Note that $\mathbf{v}^a = (-3.0, -2.3)^T$ m s^{-1} is the local minimum in the smooth area of J_{o1}/n in Fig. 2a.

the smoothness and convexity (that is, concave upwards) of the costfunction in the vicinity of the global minimum.

3. Illustrative examples

3.1. Examples with idealized observations

In this section, we assume that the true velocity $\mathbf{v}_h$ in (2) is horizontally uniform at the vertical level where the radial-velocity observations are collected along a circle at constant radial range. We also assume that the elevation angle of this range circle is small, say, $\theta = 1.5°$, so the observation operator in (2) reduces to $\mathbf{h}^T = \cos\theta(\sin\phi, \cos\phi, 0)^T$ approximately. In this case, we only need to consider the two horizontal components of $\mathbf{v}_h$, and thus simply set $u = v = 15$ m s^{-1} to represent a strong southwesterly flow. The true v_r computed from (2) with the above reduced $\mathbf{h}^T$ and uniform (u, v) is plotted as a function of ϕ by the solid curve in Fig. 1.

Idealized radial-velocity observations are generated by addition random errors to the true v_r at each observation point and then applying the aliasing operator $Z[(\ ), v_N]$ according to (1). The observation points are spaced at 1° intervals on the range circle and the azimuthal resolution is 1°, which is similar to that of the operational WSR-88D radars. The observation error standard deviation is set to $\sigma_o = 2$ m s^{-1}, which is in the range of the estimated values (not shown) from six operational WSR-88D radars (KINX, KLZK, KSGF, KSRX, KTLX and KVNX) in the central U.S. by using the innovation method of Xu et al. (2007). The Nyquist velocity is set to $v_N = 12$ (or 24) m s^{-1} to represent the typical value used for clear (or stormy) weather. The idealized radial-velocity observations generated from the above true v_r with $v_N = 12$ m s^{-1} and $\sigma_o = 2$ m s^{-1} are plotted by the dots in Fig. 1.

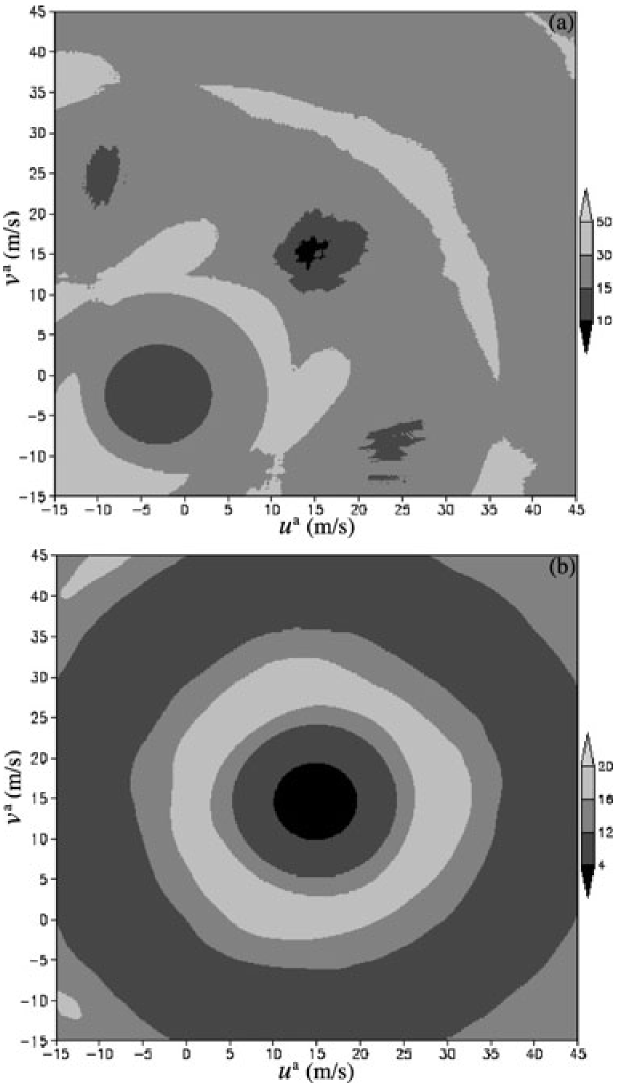

Fig. 2. Normalized observation terms J_{o1}/n in (a) and J_{o2}/n in (b). The global minimum of J_{o1}/n is 7.87 at $\mathbf{v}^a = (14.3, 16.1)^T$ m s^{-1} in (a). The global minimum of J_{o2}/n is 1.03 at $\mathbf{v}^a = (14.8, 14.6)^T$ m s^{-1} in (b). The true state point is at $\mathbf{v} = (15, 15)^T$ m s^{-1}. Note that J_{o1}/n and J_{o2}/n are in different ranges and thus plotted with different grey scales in the two panels.

For the idealized example considered in this section, the true state is a two-dimensional vector and thus can be simply denoted by $\mathbf{v} = (u, v)^T$. The analysis state vector can be then written as $\mathbf{v}^a = (u^a, v^a)^T$ and therefore $v_r^a = \mathbf{h}^T\mathbf{v}^a = (u^a\sin\phi + v^a\cos\phi)\cos\theta$. By substituting this into (4) and (6), the normalized observation terms J_{o1}/n and J_{o2}/n are computed as functions of (u^a, v^a) and plotted in Figs 2a and b, respectively, where n (= 360) is the number of observations along the selected range circle. If J_{o1} (or J_{o2}) is well formulated for aliased observations, then the

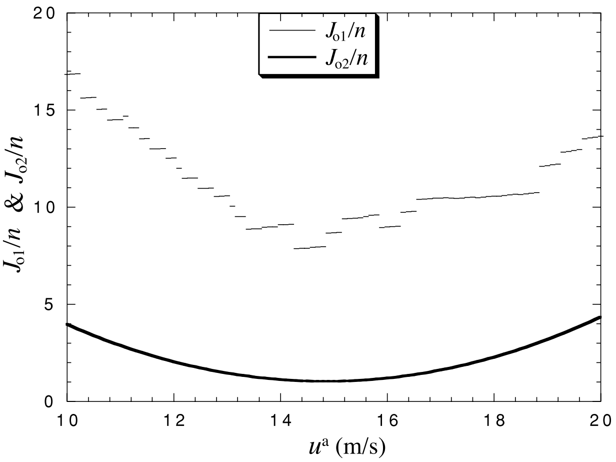

Fig. 3. J_{o1}/n and J_{o2}/n plotted by thin and thick curves, respectively, as functions of u^a with v^a fixed at their respective global minimum points (shown in Fig. 2a and 2b, respectively). The thin curve is discontinuous and it reveals the irregular fine-structure discontinuities of J_{o1}.

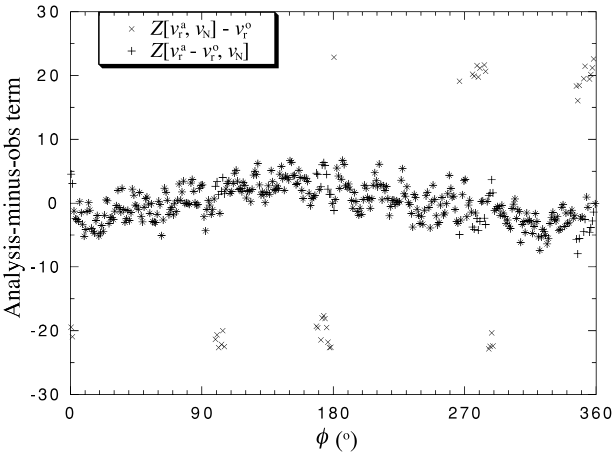

Fig. 4. Analysis-minus-observation term, $Z[v_r^a, v_N] - v_r^o$, used by J_{o1} in (4) for $\mathbf{v}^a = (16, 12)^T$ m s^{-1} plotted by × signs. Analysis-minus-observation term, $Z[v_r^a - v_r^o, v_N]$, used by J_{o2} in (6) for $\mathbf{v}^a = (16, 12)^T$ m s^{-1} plotted by + signs.

fitting residuals at the global minimum should have about the same variance as the observation errors, and this means that the global minimum should to be very close to unity. As shown in Fig. 2a, the global minimum of J_{o1}/n is 7.87 at $\mathbf{v}^a = (14.3, 16.1)^T$ m s^{-1}. This global minimum is much larger than unity and the global minimum point is deviated from the true state point at $\mathbf{v} = (15, 15)^T$ m s^{-1} significantly, so J_{o1} is not well formulated for aliased observations. On the other hand, as shown in Fig. 2b, the global minimum of J_{o2}/n is 1.03 at $\mathbf{v}^a = (14.8, 14.6)^T$ m s^{-1}. This global minimum point is close to the true state point and the global minimum is very close to unity, so the fitting residuals are statistically consistent with the observation errors and J_{o2}/n is well formulated for aliased observations.

From Fig. 2b, we can also see that J_{o2} is smooth and locally concave upwards surrounding the global minimum. The concave area is encircled by a circular ridge whose radial distance from the true state point is approximately $|\mathbf{v}^a - \mathbf{v}| \approx v_N$. Outside the concave area, there is a circular trough (shown by the dark outer ring in Fig. 2b) whose radial distance from the true state point is approximately $|\mathbf{v}^a - \mathbf{v}| \approx 2v_N$, and there are multiple local minima along this circular trough. On the contrary, as shown in Fig. 2a, J_{o1}/n is non-smooth and contains irregular fine-structure discontinuities in the area where $|\mathbf{v}^a| > v_N$, and there are multiple local minima even in the vicinity of the global minimum (shown by the irregular black area in Fig. 2a). In Fig. 3, J_{o1}/n and J_{o2}/n are plotted by the thin and thick curves, respectively, as functions of u^a with v^a fixed at their respective global minimum points. The plotted curves clearly reveal the irregular fine-structure discontinuities of J_{o1} and the smoothness of J_{o2} in the vicinities of their respective global minimum points. From (4) and (5), it is easy to see that $\sigma_o^2 J_{o1}/n$ jumps by $4v_N[v_N \pm (\Delta v_r + \varepsilon^b - \varepsilon^o)]/n$ whenever the variation of u^a (or v^a) causes $Z[v_r^a, v_N] - v_r^o$ to jump by $\pm 2v_N$ at an observation point. This quantifies how the irregular fine-structure discontinuities of J_{o1} are caused by the random observation errors and zigzag discontinuities of the aliasing operator. If the observations become perfectly error-free with $\varepsilon^o = 0$, then $\sigma_o^2 J_{o1}$ will contain only rather regular stairwise jumps (not shown) and each jump is determined by $4v_N[v_N \pm (\Delta v_r + \varepsilon^b)]$ at the observation point where $Z[v_r^a, v_N] - v_r^o$ jumps by $\pm 2v_N$ [because ε^b is independent of $\mathbf{v}^a = (u^a, v^a)$ and $\Delta v_r = \mathbf{h}^T(\mathbf{v}^a - \mathbf{v}^b)$ is a regular function of $\mathbf{v}^a$].

To see how the irregular fine-structure discontinuities of J_{o1} are generated, the analysis-minus-observation term, $Z[v_r^a, v_N] - v_r^o$, used by J_{o1} in (4) is plotted for $\mathbf{v}^a = (16, 12)^T$ m s^{-1} as an example by the × signs in Fig. 4. As a counterpart example, the analysis-minus-observation term, $Z[v_r^a - v_r^o, v_N]$, used by J_{o2} in (6) is plotted also for $\mathbf{v}^a = (16, 12)^T$ m s^{-1} by the + signs in Fig. 4. As shown, the + signs are distributed well within the range of $\pm v_N$, but the × signs jump beyond the range of $\pm v_N$ at dozens of observation points where v_r^o is aliased but $Z[v_r^a, v_N]$ is not aliased or vice versa [see the dotted curve of $v_r^a = \mathbf{h}^T\mathbf{v}^a$ for $\mathbf{v}^a = (16, 12)^T$ m s^{-1} in Fig. 1]. As $\mathbf{v}^a$ changes continuously, $Z[v_r^a, v_N] - v_r^o$ jumps discontinuously at each involved observation point. This causes irregular fine-structure discontinuities of J_{o1} in the space of $\mathbf{v}^a$. Note that $|v_r^a| \leq |\mathbf{v}^a|$, so $Z[v_r^a, v_N]$ is not aliased when $|\mathbf{v}^a| < v_N$. This explains why J_{o1} becomes smooth in the area of $|\mathbf{v}^a| < v_N$ as shown in Fig. 2a. In this smooth area, there is a local minimum at $\mathbf{v}^a = (-3.0, -2.3)^T$ m s^{-1}. The associated $v_r^a = \mathbf{h}^T\mathbf{v}^a$ is plotted in Fig. 1 by the dashed curve. When the amplitude of the curve increases (or decreases), the fitting to the aliased observations in the ±45° vicinities of $\phi \approx 45°$ and 225° becomes slightly better (or significantly worse) but the fitting to the non-aliased observations in the ±45° vicinities of $\phi \approx 135°$ and 315° becomes significantly worse (or only slightly better). This explains how the dashed curve fits the observations in the sense of least squares and why $\mathbf{v}^{\mathrm{a}} = (-3.0, -2.3)^{\mathrm{T}}$ m s^{-1} is a local minimum.

The background term in the costfunction has the following form:

$$J_{\mathrm{b}} = \sigma_{\mathrm{b}}^{-2}|\Delta\mathbf{v}|^2, \tag{9}$$

where σ_{b}^2 is the background error variance, $\mathbf{v}^{\mathrm{b}} = (u^{\mathrm{b}}, v^{\mathrm{b}})^{\mathrm{T}}$ is the background state vector, $\Delta\mathbf{v} = \mathbf{v}^{\mathrm{a}} - \mathbf{v}^{\mathrm{b}}$ is the analysis increment, the background errors are assumed to be isotropic and thus uncorrelated between the u and v components (see appendix of Xu and Wei, 2001), and the error decorrelation length scale is assumed implicitly to be infinity large (see Xu et al., 2006; their section 5a). Since J_{b} is a parabolic function of $\Delta\mathbf{v}$, the costfunction $J_{\mathrm{b}} + J_{\mathrm{o1}}$ (or $J_{\mathrm{b}} + J_{\mathrm{o2}}$) is complicated only by the observation term J_{o1} (or J_{o2}) in the presence of aliasing. As the observation term J_{o1} in (4) is discontinuous in the space $\mathbf{v}^{\mathrm{a}}$ or $\Delta\mathbf{v}$, the global minimum of $J_{\mathrm{b}} + J_{\mathrm{o1}}$ cannot be found reliably by a descent algorithm, and similar situations were seen for other types of discontinuous costfunction (Xu, 1997; Xu and Gao, 1999). On the other hand, since the observation term J_{o2} in (6) is differentiable and concave upwards as long as $|\Delta v_{\mathrm{r}} + \varepsilon^{\mathrm{b}} - \varepsilon^{\circ}| < v_{\mathrm{N}}$ at each observation point according to (8), a descent algorithm can be used to find the global minimum of $J_{\mathrm{b}} + J_{\mathrm{o2}}$ if the first guess provided by the background state $\mathbf{v}^{\mathrm{b}}$ is sufficiently close to the true state $\mathbf{v} = (15, 15)^{\mathrm{T}}$ m s^{-1}. The required closeness of $\mathbf{v}^{\mathrm{b}}$ to $\mathbf{v}$ is quantified below.

When the background state is taken to be the first guess, we have $\Delta\mathbf{v} = 0$ and $\Delta v_{\mathrm{r}} + \varepsilon^{\mathrm{b}} = \varepsilon^{\mathrm{b}} = v_{\mathrm{r}}^{\mathrm{b}} - v_{\mathrm{r}} = \mathbf{h}^{\mathrm{T}}(\mathbf{v}^{\mathrm{b}} - \mathbf{v})$. Substituting this into the required condition of $|\Delta v_{\mathrm{r}} + \varepsilon^{\mathrm{b}} - \varepsilon^{\circ}| < v_{\mathrm{N}}$ in (8) gives

$$|\mathbf{h}^{\mathrm{T}}(\mathbf{v}^{\mathrm{b}} - \mathbf{v}) - \varepsilon^{\circ}| < v_{\mathrm{N}} \text{ at each observation point.} \tag{10}$$

Note that $|\mathbf{h}^{\mathrm{T}}(\mathbf{v}^{\mathrm{b}} - \mathbf{v}) - \varepsilon^{\circ}|^2 \le |\mathbf{h}^{\mathrm{T}}(\mathbf{v}^{\mathrm{b}} - \mathbf{v})|^2 + |\varepsilon^{\circ}|^2 \le |\mathbf{h}|^2|\mathbf{v}^{\mathrm{b}} - \mathbf{v}|^2 + |\varepsilon^{\circ}|^2 = |\mathbf{v}^{\mathrm{b}} - \mathbf{v}|^2 + |\varepsilon^{\circ}|^2$, where $|\mathbf{h}|^2 = \sin^2\theta + \cos^2\theta = 1$ is used, so (10) is satisfied as long as

$$|\mathbf{v}^{\mathrm{b}} - \mathbf{v}|^2 < v_{\mathrm{N}}^2 - |\varepsilon^{\circ}|^2 \text{ at each observation point.} \tag{11}$$

As a Gaussian random variable with zero mean and a standard deviation of σ_{o}, the probability of $|\varepsilon^{\circ}| > 2\sigma_{\mathrm{o}}$ is less than 5%. Thus, (11) can be largely (with a probability >95%) satisfied if

$$|\mathbf{v}^{\mathrm{b}} - \mathbf{v}| < \left(v_{\mathrm{N}}^2 - 4\sigma_{\mathrm{o}}^2\right)^{1/2}. \tag{12}$$

This condition can be used to quantify the required closeness of $\mathbf{v}^{\mathrm{b}}$ to $\mathbf{v}$.

Note from (9) that the gradient of J_{b} is zero at $\Delta\mathbf{v} = 0$, so the costfunction gradient is determined by the gradient of the observation term at the starting point of $\mathbf{v}^{\mathrm{a}} = \mathbf{v}^{\mathrm{b}}$. Thus, as long as the background state is in the concave area encircled by the circular ridge in Fig. 2b, the descent should converge to the global minimum. For $v_{\mathrm{N}} = 12$ m s^{-1} and $\sigma_{\mathrm{o}} = 2$ m s^{-1}, the condition in (12) is $|\mathbf{v}^{\mathrm{b}} - \mathbf{v}| < 11.3$ m s^{-1} $\approx v_{\mathrm{N}}$ and this condition is consistent with the concave area in Fig. 2b. This condition can be largely (with a probability >95%) satisfied if $\sigma_{\mathrm{b}} \le (v_{\mathrm{N}}^2 - 4\sigma_{\mathrm{o}}^2)^{1/2}/2 \approx v_{\mathrm{N}}/2 = 6$ m s^{-1}. By assuming $\sigma_{\mathrm{b}} = 5$ m s^{-1} for the background term in (9), different background states are selected arbitrarily in the vicinity of the true state within the range of $|\mathbf{v}^{\mathrm{b}} - \mathbf{v}| < 12$ m s^{-1} (which is slightly larger than $2\sigma_{\mathrm{b}}$). Starting from each selected background state, the standard conjugate-gradient descent algorithm (Golub and Van Loan, 1983; their chapter 10) is used to minimize $J_{\mathrm{b}} + J_{\mathrm{o1}}$ and $J_{\mathrm{b}} + J_{\mathrm{o2}}$ with the costfunction gradients with respect to $\mathbf{v}^{\mathrm{a}} = (u^{\mathrm{a}}, v^{\mathrm{a}})^{\mathrm{T}}$ computed by

$$\nabla(J_{\mathrm{b}} + J_{\mathrm{o1}}) = 2\sigma_{\mathrm{b}}^{-2}\Delta\mathbf{v} + 2\sigma_{\mathrm{o}}^{-2}\sum_i \left(Z\left[v_{\mathrm{r}}^{\mathrm{a}}, v_{\mathrm{N}}\right] - v_{\mathrm{r}}^{\mathrm{o}}\right)_i \mathbf{h}_i \tag{13a}$$

and $$\nabla(J_{\mathrm{b}} + J_{\mathrm{o2}}) = 2\sigma_{\mathrm{b}}^{-2}\Delta\mathbf{v} + 2\sigma_{\mathrm{o}}^{-2}\sum_i \left(Z\left[v_{\mathrm{r}}^{\mathrm{a}} - v_{\mathrm{r}}^{\mathrm{o}}, v_{\mathrm{N}}\right]\right)_i \mathbf{h}_i, \tag{13b}$$

respectively, where $\mathbf{h}_i = \cos\theta(\sin\phi_i, \cos\phi_i)^{\mathrm{T}}$. As shown in Fig. 5, the descent of $J_{\mathrm{b}} + J_{\mathrm{o1}}$ fails to converge and stops at various different places in the space of $\mathbf{v}^{\mathrm{a}}$ for different starting points of $\mathbf{v}^{\mathrm{b}}$. The zigzag fluctuations of the plotted contours manifest the irregular fine-structure discontinuities of $J_{\mathrm{b}} + J_{\mathrm{o1}}$, and the implication is that the local gradient computed at an estimated point of $\mathbf{v}^{\mathrm{a}}$ by the descent algorithm can be very different from the coarse-grain gradient of $J_{\mathrm{b}} + J_{\mathrm{o1}}$. This explains why paths A, B, C and D in Fig. 5 are much more tangent than perpendicular to the coarse-grain contours and why path D can even go up from point 1 to 2 against the coarse-grain gradient. A similar failure of descent was seen in fig. 6 of Xu and Gao (1999) for a discontinuous costfunction. On the other hand, the minimization of $J_{\mathrm{b}} + J_{\mathrm{o2}}$ always converges (in 2–8 steps) to the same global minimum point at $\mathbf{v}^{\mathrm{a}} = (14.8, 14.6)^{\mathrm{T}}$ m s^{-1} (not shown), and the global minimum is $\min(J_{\mathrm{b}} + J_{\mathrm{o2}}) = 371$. This global minimum is very close to the total number (=360) of the observations and thus satisfies the optimality consistency criterion (Desroziers and Ivanov, 2001).

When the conjugate-gradient descent algorithm is used to minimize $J_{\mathrm{b}} + J_{\mathrm{o}}$ with J_{o} given as in (3), the algorithm converges to the same minimum of $\min(J_{\mathrm{b}} + J_{\mathrm{o}}) = 3670$ at $\mathbf{v}^{\mathrm{a}} = (-3.0, -2.3)^{\mathrm{T}}$ m s^{-1}. This $\mathbf{v}^{\mathrm{a}}$ is clearly a false estimate of the true state $\mathbf{v} = (15, 15)^{\mathrm{T}}$ m s^{-1}, and the minimum value is much larger than the total number of the observations and thus does not satisfy the optimality consistency criterion. If 50% of the aliased observations are dealiased, then the minimum point of $J_{\mathrm{b}} + J_{\mathrm{o}}$ moves to $\mathbf{v}^{\mathrm{a}} = (6.0, 6.1)^{\mathrm{T}}$ m s^{-1}, which is closer to the true state but still a false estimate.

3.2. *Examples with real radar observations*

In this section, real radar observations are selected from the radial velocities scanned by the operational KMHX radar at 1959 UTC on 18 September 2003 when the long-lived

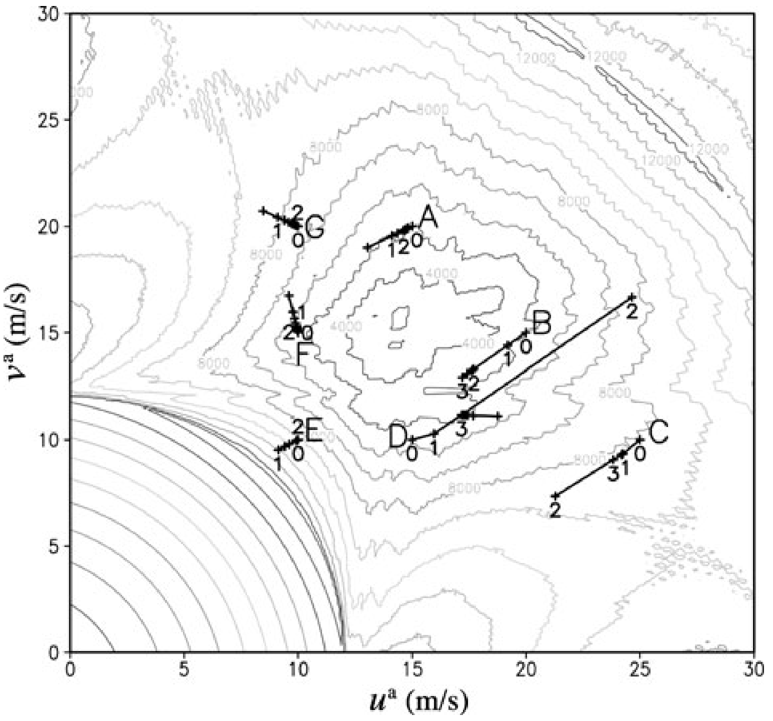

Fig. 5. Contours of $J_b + J_{o1}$ in the vicinity of the global minimum, and searching paths of failed minimization from seven different starting points: A, B, C, D, E, F and G at (u^a, v^a) = (u^b, v^b) = (15, 20), (20, 15), (25, 10), (15, 10), (10, 10), (10, 15) and (10, 20) m s^{-1}, respectively. Each path is plotted by a sequence of + signs connected by solid lines. For clarity, only the initial point and first two steps are labelled along each path by 0, 1 and 2, respectively. The total number of searching steps varies between 6 and 25 and the costfunction value at the ending step varies between 4258 and 9108 for different paths.

hurricane Isabel made landfall near Drum Inlet, North Carolina. At this time, the hurricane centre was very close to the KHMX radar location and the observed radial velocities were severely aliased even though the Nyquist velocity was as large as $v_N = 23.19$ ms^{-1}, as shown by the two horizontal grey dotted lines in Fig. 6 along with the observations (shown by dots) selected along the range circle of $r = 100$ km at the 0.5° elevation angle. The observations have a spatial resolution of 250 m in the radial direction and 1° in the azimuthal direction. The observation error standard deviation is set to $\sigma_o = 2$ m s^{-1}, which is in the range of the estimated values from the operational WSR-88D radars as mentioned in Section 3.1. As an illustrative example, only one range circle of radial-velocity observations is selected, as shown by the dots in Fig. 6.

It is easy to see from Fig. 6 that the KMHX observed radial velocities were aliased over the azimuthal ranges of $11° < \phi < 56°$ and $248° < \phi < 336°$. Although the aliased velocities can be easily identified by a human expert and corrected manually, detecting and correcting all the aliased radial velocities on each tilt of radar scans can be very challenging for an automated dealiasing algorithm, especially if the algorithm is required to be computationally very efficient for real-time operational applications. For the radial velocities scanned by the KMHX radar at the 0.5° tilt in this example, the operational dealiasing algorithm (Eilts and Smith, 1990) failed in two sector areas between $90° < \phi < 120°$ and $278° < \phi < 294°$ (not shown).

The background field is provided by the forecast produced by the Navy's Coupled Ocean/Atmosphere Mesoscale Prediction System (COAMPS®[1], Hodur 1997). The COAMPS is configured with three nested domains with resolutions of 54, 18 and 6 km for the coarse, medium and fine grids, respectively, and 30 levels in the vertical. The model configuration and nested model domains are the same as that used in section 3b of Zhao et al. (2008) for assimilating radar observations to improve the short-term storm prediction for the 2003 hurricane Isabel case. The predicted wind fields on the 6 km grid (from the control run initialized by the COAMPS analysis at 1200 UTC with the conventional observations only without including the radar observations) are projected onto the aforementioned range circle to obtain the background field (shown by the thick grey curve in Fig. 6). The background field is interpolated to $n = 120$ gridpoints evenly distributed over the entire circle with a resolution of 3° in the azimuthal angle (or 5.24 km in the azimuthal arc length for $r = 100$ km). The background wind error covariances were previously estimated for COAMPS forecasts on the same nested grids and used for the illustrative examples in Xu (2007). The rotational and divergent parts of the background vector velocity error variance were found to be roughly the same. The estimated error variance was $\sigma_b^2 = 70$ m^2 s^{-2} and the estimated de-correlation length was $L = 40$ km. These estimates will be used for the illustrative example in this section.

When the rotational and divergent parts of the background vector velocity error covariance have the same variance and

---

[1] COAMPS® is a registered trademark of the Naval Research Laboratory.

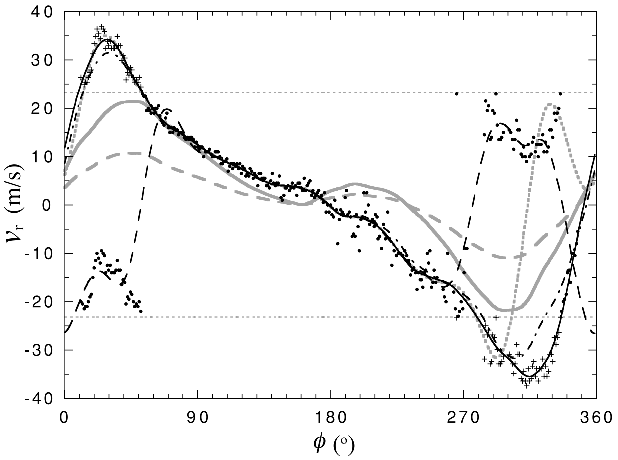

Fig. 6. KHMX radar observed radial velocities plotted by dots along the range circle of $r = 100$ km at the 0.5° elevation angle from hurricane Isabel at 19:59:47 UTC on 18 September 2003. The Nyquist interval is shown by the grey dotted lines at $v_r = \pm v_N$ with $v_N = 23.19$ m s^{-1}. The + signs plot the alias-corrected observations outside the Nyquist interval. The thick grey curve is the background radial velocity v_r^b. The thin dashed and solid curves are the analysed radial-velocity fields obtained from the minimizations of $J_b + J_{o1}$ and $J_b + J_{o2}$, respectively. The dashed grey curve is the 50% reduced v_r^b. The dotted grey and thin dash–dotted curves are the analysed radial-velocity fields obtained with the reduced v_r^b from the minimization of $J_b + J_{o2}$ constrained by all the observations and by merely the filtered observations [see (18b)], respectively. As an optimal estimate of the true state, the solid curve is constrained by all the observations and is denoted by v_r^e in the text.

de-correlation length, the background radial-velocity error covariance can be modelled by $C_b = \sigma_b^2(\cos\Delta\phi)\exp[-|\Delta\mathbf{x}|^2/(2L^2)]$, according to (3.2) and (5.7) of Xu and Gong (2003), where $\Delta\phi$ and $\Delta\mathbf{x}$ are the azimuthal separation and horizontal distance between the two correlated points. Note that the background radial velocities considered here are all along the same range circle of $r = 100$ km, so $\Delta\mathbf{x} = 2r\sin(\Delta\phi/2)$. Substituting this into the above background radial-velocity error covariance model gives

$$C_b(\Delta\phi) = \sigma_b^2(\cos\Delta\phi)\exp[-r^2\sin^2(\Delta\phi/2)/L^2]. \tag{14}$$

This error covariance model is used with the above estimates of $\sigma_b^2 = 70$ m^2 s^{-2} and $L = 40$ km to compute the background error covariance matrix $\mathbf{B}$. The background term can be written into the following form:

$$J_b = \Delta\mathbf{a}^T\mathbf{B}^{-1}\Delta\mathbf{a} = \mathbf{s}^T\mathbf{s}, \tag{15}$$

where $\Delta\mathbf{a}$ is the analysis increment vector composed of the values of $\Delta v_r = v_r^a - v_r^b$ at the background gridpoints on the entire circle, and $\mathbf{B}^{1/2}\mathbf{s} = \Delta\mathbf{a}$. As shown in Xu et al., (2006), the analysis increment vector can also include the tangential velocity field in the background term, but this inclusion does not affect the radial-velocity analysis due to the absence of tangential velocity observation. For simplicity, the tangential-velocity analysis increment is not formulated into the background term in (15). By transforming the control variable from $\Delta\mathbf{a}$ to $\mathbf{s}$, the background term is preconditioned in the last step of (15). The observation term still can be formulated in three ways as in (3), (4) and (6), except that v_r^a is computed by $\mathbf{Ha} = \mathbf{H}(\mathbf{b} + \Delta\mathbf{a}) = \mathbf{H}(\mathbf{b} + \mathbf{B}^{1/2}\mathbf{s})$, where $\mathbf{a}$ and $\mathbf{b}$ are the analysis and background state vectors composed of the values of v_r^a and v_r^b, respectively, on the analysis grid (with 120 points evenly distributed over the entire circle), and $\mathbf{H}$ is a matrix observation operator for the interpolation from the analysis grid to the observation points.

Starting from the above background state, the conjugate-gradient descent algorithm is used to minimize $J_b + J_{o1}$ and $J_b + J_{o2}$, with the costfunction gradients with respect to $\mathbf{s}$ computed by

$$\nabla(J_b + J_{o1}) = 2\mathbf{s} + 2\sigma_o^{-2}(\mathbf{HB}^{1/2})^T\mathbf{z}_1 \tag{16a}$$

$$\text{and } \nabla(J_b + J_{o2}) = 2\mathbf{s} + 2\sigma_o^{-2}(\mathbf{HB}^{1/2})^T\mathbf{z}_2, \tag{16b}$$

respectively, where $\mathbf{z}_1$ and $\mathbf{z}_2$ are the analysis-minus-observation vectors composed of $(Z[v_r^b, v_N] - v_r^o)_i$ and $(Z[v_r^b - v_r^o, v_N])_i$, respectively, for $i = 1, 2, \ldots n$ in the observation space. The minimization of $J_b + J_{o1}$ converges in 50 steps to a local minimum of the costfunction, that is, Lmin$(J_b + J_{o1}) = 2770$. This local minimum is much larger than the total number (= 318) of the observations and thus does not satisfy the optimality consistency criterion. As shown by the thin dashed curve in Fig. 6, the analysed radial-velocity field at this local minimum tends to fit the aliased observations (shown by dots) rather than the alias-corrected observations (shown by + signs) outside the Nyquist interval. Clearly, the minimization of $J_b + J_{o1}$ fails to find the global minimum. On the other hand, the minimization of $J_b + J_{o2}$ converges in 40 steps to the global minimum, that is, Gmin$(J_b + J_{o2}) = 408$. This global minimum is reasonably close to the total number of the observations. (Note that the global minimum can become very close to the total number of the observations and thus better satisfy the optimality consistency criterion if the observation error variance is tuned from $\sigma_o^2 = 4$ to 5 m^2 s^{-2}). As shown by the thin solid curve in Fig. 6, the analysed radial-velocity field at this global minimum fits very closely the alias-corrected observations (shown by + signs) outside the Nyquist interval.

The analysed radial-velocity field at the global minimum of $J_b + J_{o2}$ is an optimal estimate of the true state v_r. This estimate is constrained by all the observations and can be denoted by v_r^e. The error covariance of v_r^e can be estimated by $[\mathbf{B}^{-1} + (\sigma_o^2\mathbf{H}^T\mathbf{H})^{-1}]^{-1} \approx \sigma_o^2(\mathbf{I} - \sigma_o^2\mathbf{B}^{-1})$ and the error standard deviation is $\sigma_e \approx \sigma_o(1 - \sigma_o^2/\sigma_b^2)^{1/2} \approx 1.4$ m s^{-1}, where $\mathbf{H}^T\mathbf{H} \approx \mathbf{I}$ and $\sigma_o^2 = 2$ m^2 s^{-2} $\ll \sigma_b^2 = 70$ m^2 s^{-2} are used. Since $\sigma_e \ll \sigma_b$ (= 8.4 m s^{-1}), v_r^e can be used approximately as the true state v_r to compute the error of v_r^b, that is, $\varepsilon^b = v_r^b - v_r \approx v_r^b - v_r^e$, where v_r^b is viewed as a realization (or ensemble member) sampled from the probability distribution (or ensemble) of background fields. As shown in Fig. 6, this v_r^b is not close to v_r^e. The along-circle spatial mean of $v_r^b - v_r^e \approx \varepsilon^b$ is only 2.4 m^2 s^{-2}, but the spatially averaged rms error is as large as 8.6 m s^{-1} which is slightly larger than the estimated σ_b (= 8.4 m s^{-1}). The maximum error is $\varepsilon^b \approx v_r^b - v_r^e = 19.7$ m s^{-1} at $\theta = 326°$ which is smaller than the Nyquist velocity ($v_N = 23.19$ m s^{-1}). Thus, the condition required in (8) with $\Delta v_r = 0$ [also see (10)] is satisfied, that is,

$$\max|\varepsilon^b| \approx \max|\varepsilon^b - \varepsilon^o| < v_N. \tag{17}$$

This explains why the descent minimization of $J_b + J_{o2}$ converges to the global minimum.

The COAMPS radar data assimilation system contains a radar data quality control package (Zhao et al., 2006, 2008). In this package, the dealiasing algorithm is similar to the three-step dealiasing technique of Gong et al. (2003) except that the COAMPS forecast background wind is used for the reference check. The reference check accepts an observed or dealiased radial velocity only if it is within $\pm 0.5 v_N$ of the reference radial velocity provided by the COAMPS forecast. For the KMHX observed radial velocities in Fig. 6, this threshold condition (± 11.595 m s^{-1}) cannot be satisfied over five azimuthal ranges (between $13° \le \phi \le 38°$, $222° \le \phi \le 225°$, $234° \le \phi \le 243°$, $303° \le \phi \le 304°$ and $309° \le \phi \le 340°$). This implies that the proposed approach not only skips the dealiasing step in radar data quality control but also outperforms the existing dealiasing algorithm in the COAMPS radar data assimilation system as long as the COAMPS forecast background wind field satisfies the required condition in (17).

Now we consider that the above v_r^b is reduced by 50% (as shown by the dashed grey curve in Fig. 6) and thus becomes further away from v_r^e. The spatially averaged rms error is then increased from 8.6 to 13.5 m s^{-1} and the maximum error is $\varepsilon^b \approx v_r^b - v_r^e = 26.7$ m s^{-1} at $\phi = 320°$. In this case, the condition (17) is no longer satisfied, so the descent minimization of $J_b + J_{o2}$ fails to converge to the global minimum. Instead, it converges to a local minimum. The analysed radial-velocity field v_r^a at this local minimum is plotted by the dotted grey curve in Fig. 6. As shown, this v_r^a is deviated from v_r^e (thin solid curve) sharply over the range of $310° < \phi < 350°$ in the vicinity of the maximum error ($\varepsilon^b \approx 26.7$ m s^{-1} at $\phi = 320°$) where (17) is violated. Note that ε^b reaches the negative maximum of –24.7 m s^{-1} at $\phi = 27°$ and thus also goes beyond $\pm v_N$ over the narrow range of $19° < \phi < 27°$, but the analysis v_r^a is only slightly deviated from v_r^e over this narrow range.

The condition (17) can be relaxed to

$$\max|\varepsilon^b| \approx \max|\varepsilon^b - \varepsilon^o| < (1+\alpha)v_N \tag{18a}$$

if the observations are filtered by the following threshold:

$$|Z\left[v_r^b - v_r^o, v_N\right]| \le (1-\alpha)v_N, \tag{18b}$$

where α is a constant between 0 and 1. When $\alpha \to 0$, (18a) reduces to (17), and (18b) is trivially satisfied by all the observations. When $\alpha \to 1$, (18b) tends to reject all the observations and thus nullify (18a). The error of the reduced v_r^b does not satisfy (17) but satisfies the relaxed condition (18a) at least with $\alpha =$ 0.5. By using the observations filtered by (18b) with $\alpha = 0.5$, the minimization of $J_b + J_{o2}$ converges to the global minimum constrained merely by the filtered observations. As shown by the thin dash–dotted curve in Fig. 6, the analysed radial-velocity field v_r^a at this minimum is closer to v_r^e (solid curve) than v_r^b (thick grey curve). This v_r^a can be also obtained by minimizing the conventional costfunction $J_b + J_o$ [see (3)] after the observations are filtered by (18b) with $\alpha = 0.5$ and dealiased by using v_r^b as the reference state (see sections 2b–2c of Gong et al., 2003; section 3b of Zhao et al., 2006). Here, by minimizing the modified costfunction $J_b + J_{02}$, v_r^a is estimated directly from the filtered observations without dealiasing. This v_r^a can be used as a new initial guess in place of v_r^b in (18b) to re-filter the observations and re-minimizing $J_b + J_{o2}$ to find the global minimum constrained by the re-filtered observations. The process can be iterated until no more observations can be retrieved by re-filtering. For the above 50% reduced v_r^b with $\alpha = 0.5$, the process is completed in four iterations with all the observations retrieved and the analysis becomes very close to v_r^e (thin solid curve in Fig. 6) in the final iteration. Note that the background error variance ($\sigma_b^2 = 70$ m^2 s^{-2}) estimated for the original v_r^b is much larger than the observation variance ($\sigma_o^2 = 4$ m^2 s^{-2}). For simplicity, however, the background error variance is not adjusted (or updated) when v_r^b is reduced by 50% (or updated by the analysis during the iteration). Because of this, the analysis in the final iteration is not exactly the same as v_r^e, although the difference is too small (between –0.3 and 0.4 m s^{-1}) to show in Fig. 6.

4. Conclusions

In this paper, an aliasing operator is introduced to mimic the effect of radar radial-velocity aliasing and the resultant zigzag-discontinuities in radial-velocity observations. This aliasing operator can be incorporated into the observation term of the costfunction to facilitate direct assimilations of aliased radar radial-velocity observations in two ways. The first way treats the aliasing operator as a part of the observation operator in consistence with the conventional form of the observation term in the costfunction, but it does not ensure the analysis to be aliased (or not aliased) in consistency with the aliased (or not aliased) observation at every observation point. As a result, the analysis-minus-observation term contains a large alias error whenever an inconsistency occurs at an observation point. This causes fine-structure discontinuities in the costfunction. The second way applies the aliasing operator to the analysis-minus-observation term at each observation point. In this way, the analysis is ensured to be aliased (or not aliased) in consistency with the aliased (or not aliased) observation at each observation point as long as the difference of analysis error and observation error (not including the alias error) is within the Nyquist interval (between $\pm v_N$). The costfunction is thus smooth and concave upwards in the vicinity of the global minimum. As a unconventional approach, the second way is thus superior to the first way for assimilating aliased radar radial-velocity observations, and this is demonstrated by illustrative examples with both simulated and real radar observations.

Although the above unconventional approach ensures the smoothness and convexity (that is, concave upwards) of the costfunction in the vicinity of the global minimum, the modified costfunction is not globally convex (or concave upwards) and has multiple minima due to the zigzag-discontinuities of the aliasing operator. In this case, the global minimum cannot be solved by a direct method (derived by setting the costfunction gradient to zero) but can be found by a descent method (such as the conjugate-gradient algorithm) if the first guess (provided by the background state) is close to the true state with its maximum error smaller than the Nyquist velocity $v_{\rm N}$ [see (10) and (17)]. If the maximum error of the first guess exceeds $v_{\rm N}$ but is still well below $2v_{\rm N}$ [see (18a)], then the global minimum cannot be found by a descent method unless the costfunction is re-constructed by filtered observations [see (18b)]. When the first guess is not close to the true state with its maximum error close to or larger than $2v_{\rm N}$, the global minimum of the modified costfunction is beyond the reach of a descent method. In this case, finding the global minimum becomes very challenging and difficult especially when the dimension of the minimization problem is large. For some practical applications, the minimization problem has only a few control variables (see the examples in Section 3.1 of this paper), and an efficient method can be developed to find the global minimum of the modified costfunction even when the first guess is zero and far away from the true state. Progress made in this direction will be reported elsewhere. Furthermore, the global minimization problem in this paper can be re-derived in terms of Bayesian estimation by folding the domain of the original Gaussian non-aliased observation probability density function into the Nyquist interval (Xu, 2009), and this establishes the theoretical basis for the unconventional approach proposed in this paper.

5. Acknowledgments

The authors are thankful to Dr. Dick Doviak, Dr. David Parrish, and the anonymous reviewer for their comments and suggestions that improved the presentation of the results. The research was supported by the ONR Grant N000140410312 to the University of Oklahoma. Funding was also provided by NOAA/Office of Oceanic and Atmospheric Research under NOAA-University of Oklahoma Cooperative Agreement #NA17RJ1227, U.S. Department of Commerce.

References

Bergen, W. R. and Albers, S. C. 1988. Two- and three-dimensional dealiasing of Doppler radar velocities. *J. Atmos. Oceanic Technol.* **5**, 305–319.

Daley, R. and Barker, E. 2001. NAVDAS: formulation and diagnostics. *Mon. Wea. Rev.*, **129**, 869–883.

Desroziers, G. and Ivanov, S. 2001. Diagnosis and adaptive tuning of observation-error parameters in a variational assimilation. *Quart. J. Roy. Meteor. Soc.*, **127**, 1433–1452.

Doviak, R. J. and Zrnić, D. S. 2006. *Doppler Radar and Weather Observations*. 2nd Edition. Dover Publications, New York, 562 pp.

Eilts, M. D. and Smith, S. D. 1990. Efficient dealiasing of Doppler velocities using local environment constraints. *J. Atmos. Oceanic Technol.* **7**, 118–128.

Gao, J., Droegemeier, K. K., Gong, J. and Xu, Q. 2004. A method for retrieving mean horizontal wind profiles from single-Doppler radar observations contaminated by aliasing. *Mon. Wea. Rev.* **132**, 1399–1409.

Golub, G. H. and Van Loan, C. F. 1983. *Matrix Computations*. Johns Hopkins University Press, Baltimore, 476 pp.

Gong, J., Wang, L. and Xu, Q. 2003. A three-step dealiasing method for Doppler velocity data quality control. *J. Atmos. Oceanic Technol.* **20**, 1738–1748.

Haase, G. and Landelius, T. 2004. Dealiasing of Doppler radar velocities using a torus mapping. *J. Atmos. Oceanic Technol.* **21**, 1566–1573.

Hennington, L. 1981. Reducing the effects of Doppler radar ambiguities. *J. Appl. Meteor.* **20**, 1543–1546.

Hodur, R. M. 1997. The Naval Research Laboratory's coupled ocean/atmosphere mesoscale prediction system (COAMPS). *Mon. Wea. Rev.* **125**, 1414–1430.

James, C. N. and Houze, R. A. 2001. A real-time four-dimensional Doppler dealiasing scheme. *J. Atmos. Oceanic Technol.* **18**, 1674–1683.

Jing, Z. and Wiener, G. 1993. Two-dimensional dealiasing of Doppler velocities. *J. Atmos. Oceanic Technol.* **10**, 798–808.

Parrish, D. and Derber, J. 1992. The National Meteorological Center's spectral statistical analysis system. *Mon. Wea. Rev.* **120**, 1747–1763.

Ray, P. and Ziegler, C. 1977. Dealiasing first moment Doppler estimates. *J. Appl. Meteor.* **16**, 563–564.

Tabary, P., Scialom, G. and Germann, U. 2001. Real-time retrieval of the wind from aliased velocities measured by Doppler radars. *J. Atmos. Oceanic Technol.* **18**, 875–882.

Xu, Q. 1997. Generalized adjoint for physical processes with parameterized discontinuities. Part IV: problems in time discretization. *J. Atmos. Sci.* **54**, 2722–2728.

Xu, Q. 2007. Measuring information content from observations for data assimilation: relative entropy versus Shannon entropy difference. *Tellus* **59A**, 198–209.

Xu, Q. 2009. Bayesian perspective of the unconventional approach for assimilating aliased radar radial velocities. *Tellus* **61A**, doi:10.1111/j.1600-0870.2009.00413.x.

Xu, Q. and Gao, J. 1999. Generalized adjoint for physical processes with parameterized discontinuities. Part VI: minimization problems in multi-dimensional space. *J. Atmos. Sci.*, **56**, 994–1002.

Xu, Q. and Gong, J. 2003. Background error covariance functions for Doppler radial-wind analysis. *Quart. J. Roy. Meteor. Soc.* **129**, 1703–1720.

Xu, Q. and Wei, L. 2001. Estimation of three-dimensional error covariances. Part II: analysis of wind innovation vectors. *Mon. Wea. Rev.* **129**, 2939–2954.

Xu, Q., Liu, S, and Xue, M. 2006. Background error covariance functions for vector wind analyses using Doppler radar radial-velocity observations. *Quart. J. Roy. Meteor. Soc.* **132**. 2887–2904.

Xu, Q., Nai, K. and Wei, L. 2007. An innovation method for estimating radar radial-velocity observation error and background wind error covariances. *Quart. J. Roy. Meteor. Soc.* **133**, 407–415.

Yamada, Y. and Chong, M. 1999. VAD-based determination of the Nyquist interval number of Doppler velocity aliasing without wind information. *J. Meteor. Soc. Japan* **77**, 447–457.

Zhang, J. and Wang, S. 2006. An automated 2D multipass Doppler radar velocity dealiasing scheme. *J. Atmos. Oceanic Technol.* **23**, 1239–1248.

Zhao, Q., Cook, J., Xu, Q. and Harasti, P. 2006. Using radar wind observations to improve mesoscale numerical weather prediction. *Wea. Forecast.* **21**, 502–522.

Zhao, Q., Cook, J., Xu, Q. and Harasti, P. 2008. Improving short-term storm predictions by assimilating both radar radial-wind and reflectivity observations. *Wea. Forecast.* **23**, 373–391.